A DATA DRIVEN BASED METHODOLOGY FOR STURCTURAL HEALTH MONITORING WITH DISTRIBUTED OPTICAL FIBRE SENSORS

Zhangquan Shen[1], Yiding Liu[2,*], Anubhav Singh[3], Wenhao Li[1], Tianyu Chen[4], Shijun Guo[1] and Darren J. Hughes[3]

[1] Centre of Excellence for Aeronautics, School of Aerospace, Transport and Manufacturing, Cranfield University, MK43 0AL, UK
[2] School of Physics, Engineering & Computer Science, University of Hertfordshire, Hatfield, AL10 9AB, UK
[3] WMG, University of Warwick, Coventry, CV4 7AL, UK
[4] Key Laboratory of Microgravity (National Microgravity Laboratory), Institute of Mechanics, Chinese Academy of Sciences, Beijing 100190, China

* Corresponding author. Email address: y.liu@herts.ac.uk

Keywords: Structural Health Monitoring (SHM); Distributed Optical Fibre Sensors (DOFS); k-nearest neighbours (KNN) kernel; Deep Neural Network (DNN); Semi-supervised learning.

ABSTRACT

Structural health monitoring (SHM) is a means for maintaining structural integrity, safety and reliability by analysing various structural responses (i.e., mechanical signals) to pinpoint the anomalies of the structures due to damage. It is not an easy task to filter the noise and fluctuation of mechanical signals to successful find the damage-induced anomalies, but it might be achieved by machine learning algorithms. However, the successful implementation of a machine learning requires a large amount of training data, which is always available. In this work, a novel machine learning (ML) model, combining k-nearest neighbors kernel (KNN) and deep neural network (DNN), was proposed that can be trained by insufficient/incomplete SHM data. In addition, the damage states can be identified by Kernel Principle Component Analysis (KPCA). To demonstrate the accuracy of this model, training and validation data were taken from the strains of the braided composite beam under progressive three-point bending. The strain signals were measured by embedded distributed optical fibre sensors (DOFS). The prediction of the proposed novel ML model demonstrates a good agreement with the experimental observations for validation, which provides a novel approach for sufficient/incomplete training data.

1 INTRODUCTION

Structural Health Monitoring (SHM) is a transdisciplinary field of engineering devoted to ensuring the structural integrity and operational safety of a component or structure [1]. SHM is primarily driven by the damage detection to detect the damage at the earliest possible stage (near real-time) to extend the design basis service life of the existing structural and mechanical structures in aircraft, bridges, offshore platforms, buildings and defence systems [2]. Traditionally, the damage detection process relied on physical-based methods and parametric approaches, e.g., determination of the stiffness matrix or modal parameters [3,4], to extract meaningful information from the measured data. However, as the underlying system complexity increases (e.g., complex real-world structures, material uncertainties, environmental/operational variations), it is difficult to produce a reliable damage estimation. In fact, the monitoring and analysis of damage-sensitive features derived from raw experimental data of a monitored structure may be necessary to accurately detect structural anomalies resulting from damage [3]. Indeed, a large amount of SHM data are generated and collected which might include noise, redundant information, outliers, etc. Therefore, more efficient methodology of processing these SHM data based on the algorithms used to handle the data should also be developed [5]. All these have motivated the use

of a data-driven approach for SHM where damage assessment is handled to compensate for the challenges associated with the physical-based approach.

The last few decades have stimulated the Machine Learning (ML) techniques at building models for mapping input patterns in measured SHM data to output targets for damage assessment at different levels (e.g., establishing the presence of damage) [1]. Conventionally, supervised learning ML techniques were limited in processing the large amount of data of hand-crafted damage-sensitive features on physical-based SHM studies, for example, damage locating vector (DLV) [6,7], probabilistic reconstruction algorithm (PRA) [8]. In supervised and partially supervised approaches, there is a set of training data available, whose relationships with physical damage phenomena appear to be known. They are then applied to analyse the new datasets. Min et al. [9] proposed an innovative Neural Network (NN)-based pattern analysis tool to identify damage-sensitive frequency ranges to detect loose bolts and notches on a bolt-jointed aluminium beam and a lab-scale pipe structure. Selva et al. [10] presented a Probabilistic Neural Networks (PNNs) approach to detect and localize damage in composites Carbon Fibre Reinforced Plates (CFRPs) based on a coupled Finite Element Methods (FEM) and electromechanical impedance (EMI) techniques. However, these above damage detection systems were highly depended on the selected damage-sensitive features. In addition, these hand-crafted features may be sub-optimal for the structure under consideration, as there is no guarantee that the same set of features can be happen in the realistic situations. Whilst supervised learning is the most common form of learning, damage detection in most SHM applications is often performed in a semi-supervised or unsupervised manner since real-world structures are unlikely to have a clear description of their damage scenarios. To overcome this shortcoming, Deep learning (DL) methods have also attracted more attention as it allows raw data to be used and features to be learnt from it using a general-purpose learning process [1,11,12]. An interesting technique within the domain of unsupervised learning is clustering, which can be useful for anomaly detection. Clustering groups data points that are similar into different subsets in such a way that the normal distribution is preserved as clusters and the damage is detected using an outlier detection approach [3]. Park et al. [13] incorporated the Principal Component Analysis (PCA)-based data compression and *k*-means clustering-based pattern recognition methodology for an EMI-based SHM study and the proposed methods were effective in inspecting loose bolts in a bolt-jointed aluminium structures. Jiang et al. [14] employed *k*-means clustering analysis for a piezoelectric active sensor self-diagnosis EMI SHM problem and the results found that *k*-means clustering based on admittance characteristics can accurately distinguish and identify the structural damage for four kinds of sensor damages.

Compared to other damage detection techniques (i.e., vibration based and ultrasonic guided wave-based), the use of Distributed Optical Fibre Sensors (DOFS) for strain-based methods is appealing due to their light weight and small size, especially negligible intrusion in the host structure for composite materials. Many researchers have focused their studies on the embedment of DOFS in different production processes of thermoset composite materials (e.g., autoclave, hot press and VARIM) for manufacturing monitor and damage detection, debonding or delamination etc. [15–19]. However, most of the studies qualified the damage with a local change in the signal response without quantifying the high data flow into a state index after filtering out signals from environmental disturbances and noise. Moreover, a robust and generalizable model for the automated detection and characterization of damage is impossible to train unless sufficient data are collected and treated. Consequently, it is necessary to develop smart data-driven models to augment the insufficient/incomplete training data of real-world structures to perform higher levels of damage assessment and/or develop more comprehensive data acquisition methods, given the insufficient/incomplete training data. Semi-supervised learning strategy was found a powerful tool to integrate and associate raw data with the physical-based experimental observations using artificially labels of damage-sensitive features [20]. Normally, it takes a lot of efforts to artificially label the raw data and the way to label data may have effects on the fitting performance of neural network models. To significantly reduce the amount of artificially assigned labels as well as to interpret the material characteristics based on merely raw data sources, a data driven based new methodology was proposed in this paper.

In this paper, we firstly tested a thermoplastic braided composite beam integrated with DOFS under a three-point bending test with six defined loading-unloading cycles. The raw measured strain data from DOFS was corelated to the bearing performance of the specimen by labeling a few particular points in

the measured data sequence. Subsequently, a semi-supervised learning algorithm was employed to propagate the labels according to the data characteristics and fitted by a DNN architecture. A state index based on labels was proposed to represent the load performance and load capacity of the sample. The developed DNN architecture was capable of predicting the state index based on a sequence of raw data. The projected labels were further decomposed to the feature space and coupled with the prediction by DNN to identify the potential damage in the material, which was well supported by experimental findings.

2. Distributed optical fibre sensors (DOFS)

DOFS, as distributed optical fibre sensing, is capable of achieving the strain or temperature measurements without the use of gratings by measuring the low amplitude signal of reflected light referred to as Rayleigh backscatter [21]. Rayleigh scattering based OFS were used due to their high chemical stability and small diameter. Such fibres were embedded in the anode electrode of a prototype pouch cell to monitor the distributed strain and temperature in real-time under different operating conditions.

The Rayleigh backscatter in DOFS is caused by random fluctuations in the index profile along the fibre length, which is an inherent phenomenon in fibre during the manufacturing process. For every individual fibre, the scatter amplitude as a function of distance is a random but static property of that fibre [21,22]. If the local changes in temperature and strain are relayed to the optical fibre (OF), the scattered signal in the fibre is modulated by these physical parameters. Specific optical interrogator-based electronics utilise this scatter "fingerprint" to measure a shift between its reference state and externally stimulated state [22]. Therefore, this shift is calibrated to quantify the local physical variables of strain and temperature. The desired features of Rayleigh scattering based fibre sensing technique allows distributed measurements with millimetre-scale spatial resolution and high measurement accuracy, making it a suitable solution for in-situ applications.

Optical Frequency Domain Reflectometry (OFDR) uses polarization-devise to measure both the amplitude and phase of the Rayleigh backscatter signal [22]. In OFDR, either the optical frequency of the light source or the frequency of an amplitude modulation is swept and acquired by "coherent" and "incoherent" systems [23]. The spatial information is then retrieved by a Fourier transform to the backscatter in the frequency domain. The network of the OFDR system is shown in Figure 1. Light from a Tunable Laser Source (TLS) with linearly scanning optical frequency is split by a coupler, where one part of the light is launched as the reference and the other parts acts into the fibre under test (FUT). In the measurement path, the backscattered light from the FUT recombined with the light from the reference path and their frequency beating is acquired by a photodetector. Finally, the Fourier transform of the signal at the detectors results in the phase and amplitude of the signal as a function of length (or delay) along the sensor [22].

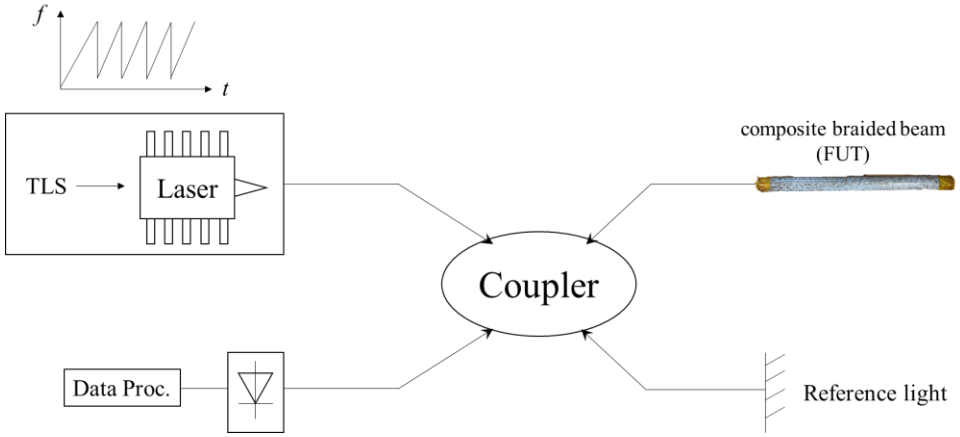

Figure 1: Basic set-up of a OFDR network. The incident light is a continuous wave with frequency sweeping; the Rayleigh backscattered light from the sensing fibre is mixed with the reference light at a photodetector, and the obtained signal is processed to retrieve the spatial information. TLS: Tunable Laser Source. FUT: Fibre under test.

Therefore, by analysing the interference signal of the main interferometer, it can be found that a specific frequency f_B, named as the beat frequency, directly corresponds to a specific position (z) along the Fibre under test (FUT). The spatial resolution (Δz) can be given as

$$\Delta z = \frac{c}{2n_g \Delta F} \quad (1)$$

where c is the speed of light in space, n_g is the group refractive index, ΔF is the frequency tuning range of the Tunable Laser Source (TLS). In known conditions, a stable and unique fingerprint Rayleigh backscattered spectrum (RBS) is acquired. The local RBS shifts in frequency when a variation in the environmental conditions occurs. A change in strain or temperature from the baseline condition results in a frequency shift in the spectrum of light scattered in the fibre. Changes in the local period of Rayleigh scattering cause temporal and spectral shifts in the locally-reflected spectrum, which can be scaled to from a distributed sensor. The strain response arises due to both the physical elongation and compression of the sensor, and the change in fibre index due to photoelastic effects [24]. The physical length and refraction index of the fibre are intrinsically sensitive to the measurement of both temperature and strain; therefore, when the external temperature in unchanged, the bare fibre sensor is used as the ε-DOFS.

3. Experimental Investigation

3.1. Manufacturing of smart thermoplastic composite beam with DOFS

The process used to produce the thermoplastic composite beams with integrated DOFS involved three steps, as shown in Figure 2. In the braiding and preform preparation, a commingled material system procured from Coats plc composed of *E*-glass fibres and polyamide 6 (PA6) filaments was used to braid the preforms. The braiding of the circular hollow preforms was performed at Composite Braiding Ltd using a 64-carier braiding machine. Three layers were overbraided on an acetal mandrel with an outer diameter of 25 mm. The machine parameters were set to achieve a target braid angle of 45° in all the braided layers.

The next step is the Integration of OF. The OF employed in this study is a polyimide coated, low bend loss, single mode fibre, which was integrated between the outermost and second layer of the braided preform. In order to protect the termination of the optical fibre, a 0.6 mm diameter Poly-Tetra-Fluoro-Ethylene (PTFE) coating was used in the ingress and egress portions. The coated portions were also secured to the second layer of the braid using masking tape to maintain orientation of the OF. Finally, the outermost layer was carefully reinstated, and a silicone rubber bladder was put through the preform. Bespoke designed metallic end fittings were attached at both ends of the bladder that would enable internal pressurisation during the moulding process.

The preforms were moulded using a novel balder moulding technique called rapid variothermal moulding (RVM) developed previously by [25]. The process uses a hydraulic press integrated with a modern smart tooling concept developed by Surface Generation Ltd. The tooling setup enables rapid heating/cooling of the mould faces while maintaining thermal uniformity across the mould via localised thermal control. The detailed moulding process was depicted in [25].

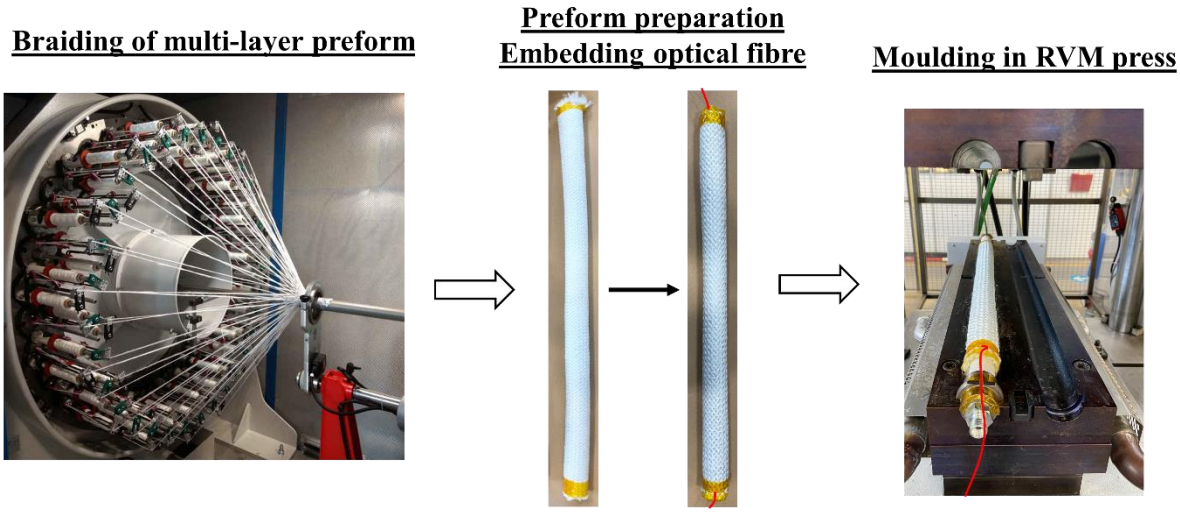

Figure 2: Key steps in manufacturing thermoplastic braided beams. Left: Braiding onto mandrel. Centre: Preparation for RVM and embedment of optical fibre. Right: Preform inside the press. The red line highlighted the insertion of DOFS.

3.2. Interrupted mechanical tests

A quasi-static three-point flexural test was conducted using an Instron 3367 test machine with a 30 kN load cell in compression mode, as shown in Figure 3(a). The support span was 350 mm, which is consistent with those tested in our previous study [25]. The separate loading-unloading interrupted test was carried out at a slower crosshead speed of 0.5 mm/min under displacement control. The strain measurements from DOFS were validated with the surface strain distribution from a three-dimensional digital image correlation (GOM 12 3D-DIC) system in our previous study. The tests were stopped at a crosshead displacement of 12 mm as significant lateral movement was observed at the beam-support roller interfaces upon deflections beyond this. The reason of loading-unloading interrupted test was mainly to determine the repeatability of strain measurements in DOFS and also to visually observe the induced damage by a travelling microscope equipped with a digital camera, as shown in Figure 3(b). Six loading-unloading cycles (defined as LC1 to LC6) selected under progressively increasing maximum displacement were decided according to the continuous test done for the samples previously, as indicated in Table 2. The Optical Frequency Domain Reflectometry (OFDR) system from the LUNA Inc. (ODiSI-B model) was used to monitor strain in the optical fibre during the test. The DOFS's acquisition rate is 1 Hz with a gage length of 1.25 mm. An X-Ray micro–Computed Tomography (micro-CT) scan was performed at the Centre for Imaging, Metrology and Additive Technologies (CiMAT) at WMG, Warwick University to extract detailed information regarding the positioning of the optical fibre within the three-dimensional volume of the specimen. The detailed X-ray micro-CT setup was introduced in our previous work. Figure 3(c) highlighted the DOFS with PTFE coating close to the end of the sample. It can be seen that the optical fibre situated with a vertical distance of 5.3 mm to the top surface where the loading created.

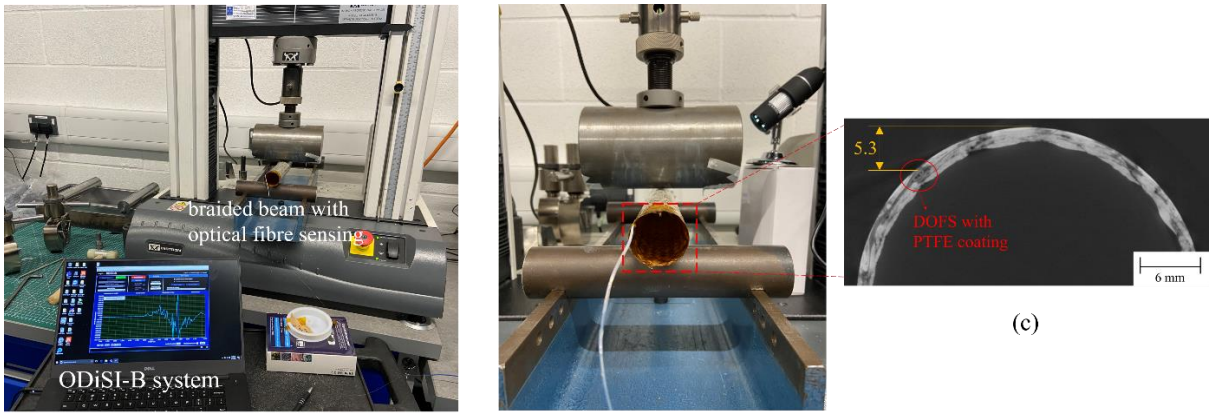

Figure 3: (a) Three-point bending experimental set up with OFDR-bases interrogator for strain measurement, (b) the traveling microscope used to measure damage during the interrupted test

Table 1 Loading-unloading cycles of interrupted three-point bending test

Loading cycle	Maximum displacement (mm)	Maximum load (N)
1	3.0	272.96
2	4.5	360.90
3	6.0	427.46
4	7.5	465.77
5	9.0	471.38
6	10.5	447.94

4. Machine learning based approaches

Machine learning technologies have merged as one of the most promising expertise thriving in the 21st century, and by the way of learning, it can be classified as supervised learning, semi-supervised learning, and unsupervised learning algorithm. For supervised learning algorithms, the data input to the model is all labelled, and the mapping relationship between inputs and outputs will be fit by the model based on the labels. For unsupervised learning algorithms, the data will be clustered according to the characteristics of the data in the feature space. For semi-supervised learning algorithms, the input data is partially labelled, and the labels of the unlabelled data were inferred from the labelled ones.

In this paper, we proposed a general prediction methodology for damage detection based on data driven models by means of raw strain measurements from DOFS using different machine learning based approaches. The schematic diagram of the proposed methodology was illustrated in Figure 4. This methodology consisted of the following steps:

(a) The load-midspan performance of the structure under different load cycles were firstly analysed;
(b) A state index S_{index} was determined based on the stiffness degradation of the structure and a few points were also artificially labelled;
(c) Semi-supervised label spreading algorithm was used to spread the labels to unassigned datapoints throughout the whole loading process;
(d) A supervised Deep Neural Network (DNN) architecture was used to fit the dataset which was formed by the original data and labels obtained in step (c) for state index prediction;
(e) Finally, the Kernel Principal Component Analysis (KPCA) algorithm was used to decompose the labels and to visualise the pattern change induced by damage in the feature space.

The methodology utilizes the excellent capability of neural networks to fit the raw strain measurement data from DOFS and the limited number of artificially labelled state index based on the experimental observations. It was further combined with KPCA to reasonably reveal the pattern change occurred during the damage evolution process in the feature space by dimension decomposition. The main advantages of this methodology lie in the ability of label spreading algorithm to reduce the demand of the artificially labelled data and the reasonable assignment of labels based on the data characteristics. The detailed learning process of label spreading, DNN and KPCA are introduced in the following sections.

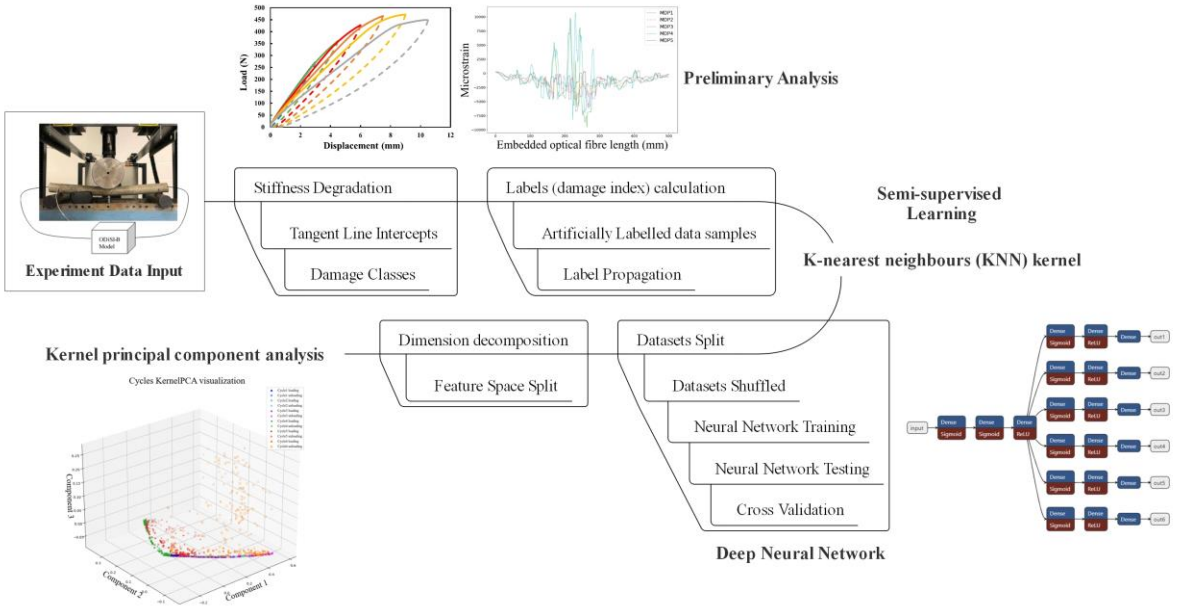

Figure 4: Schematic diagram of the proposed damage detection methodology based on machine learning approaches.

4.1. label spreading

Label spreading is a kind of semi-supervised learning technique that use label spreading algorithm to propagate the labels to the unlabelled data points when given a set of labelled data points. The principal theory of label spreading can be referenced to [26] and illustrated as follows.

Given dataset $\chi=\{x_1,\ldots,x_l,x_{l+1},\ldots,x_n\}\subset\mathbb{R}^m$, and the first p points $x_i(i\le p)$ have labels $\{y_1,\ldots,y_p\}\in\Gamma$ while the others $x_u(p+1\le u\le n)$ are unlabeled, and Γ is the label set. Let F denote a $n\times c$ matrix with nonnegative elements: $F=\begin{bmatrix}F_{11}&\cdots&F_{1c}\\ \vdots&\ddots&\vdots\\ F_{n1}&\cdots&F_{nc}\end{bmatrix}$, and labels $y_i=arg\ max_{j\le c}F_{ij}$ for each data point x_i. Let Y denote a $n\times c$ matrix representing labeled data points. For artificially labeled data point x_i and corresponding label y_i, $j=y_i$ and let $Y_{ij}=1$ otherwise $Y_{ij}=0$. The affinity matrix W is defined by $W_{ij}=\begin{cases}\exp\left(-\|x_i-x_j\|^2/2\sigma^2\right) & i\ne j\\ 0 & i=j\end{cases}$. Constructing the matrix $S=D^{-\frac{1}{2}}WD^{-\frac{1}{2}}$ in which D is the diagonal matrix with its elements on the main diagonal of the matrix $D_{ii}=\sum_{j=1}^{n}W_{ij}$

The label spreading algorithm iterate $F(t+1)=\alpha SF(t)+(1-\alpha)Y$ until convergence. Let F^* denote the limit of the sequence $\{F(t)\}$ and each point is labelled by $y_i=\arg\max_{j\le c} F_{ij}^*$.

4.2. Deep Neutral Network (DNN)

DNN is one of the research focuses of artificial intelligence technology, and its excellent ability of nonlinear fitting makes it a promising tool to deal with large quantity data [27,28]. The data input to the deep neural network will backpropagate from the lower layers to upper layers and update the parameters in the new network, the formulation of the outputs in the l^{th} layer can be represented as:

$$x_{i,j}^l=\sum_m\sum_n w_{m,n}^l o_{i+m,j+n}^{l-1}+b_{i,j}^l \tag{2}$$

4.3. Kernel Principal Component Analysis (KPCA)

KPCA method is to decompose the dimensions of the original data to specified components according to the covariance matrix and kernel function [29]. Herein, linear kernel function *K* was used to calculate KPCA. The data samples contained *N* dimensions of data and were decomposed into *K* components.

$$K(x_i,x_j)=\phi(x_i)^T\phi(x_j)=\langle x_i,x_j\rangle, i,\ j=1,\cdots,N, \tag{3}$$

Assuming that μ is the mean of the data in the feature space and we have zero mean:

$$\mu=\frac{1}{n}\sum_{i=1}^n\phi(x_i)=0, i=1,\cdots,N \tag{4}$$

The covariance matrix is calculated by:

$$C=\frac{1}{n}\sum_{i=1}^n\phi(x_i)\phi(x_i)^T, i=1,\cdots,N \tag{5}$$

Its eigenvalues and eigenvectors are given by:

$$C\upsilon=\lambda\upsilon \tag{6}$$

The above formulation can be rewritten as:

$$\frac{1}{N}\sum_{i=1}^N\phi(x_i)\{\phi(x_i)^T v_k\}=\lambda_k v_k, i=1,\cdots,N \text{ and } k=1,\cdots,K \tag{7}$$

And then v_k can be derived as:

$$v_k=\sum_{i=1}^N a_{ki}\phi(x_i), i=1,\cdots,N \text{ and } k=1,\cdots,K \tag{8}$$

Assuming matrix $K_{i,j}=K(x_i,x_j), i,\ j=1,\cdots,N$, and then the Equation can be rewritten in matrix form $K^2a_k=\lambda_k NKa_k$. For data features $\phi(x_i)$ may not have mean 0, the normalized $\tilde{\phi}(x_i)$ can be written as:

$$\tilde{\phi}(x_i)=\phi(x_i)-\frac{1}{N}\sum_{k=1}^N\phi(x_k), i=1,\cdots,N \text{ and } k=1,\cdots,K \tag{9}$$

The normalized kernel function can be written as:

$$\tilde{K}(x_j, x_k)=\tilde{\phi}(x_j)^T\tilde{\phi}(x_k)=\left(\phi(x_j)-\frac{1}{N}\sum_{i=1}^{N}\phi(x_i)\right)^T\left(\phi(x_k)-\frac{1}{N}\sum_{i=1}^{N}\phi(x_i)\right), i=1,\cdots,N \text{ and } k=1,\cdots,K \quad (10)$$

The new data point after dimensionality reduction can be represented as:

$$y_j=\sum_{i=1}^{N}a_{ji}\tilde{K}(x, x_i),\ j=1,\cdots,K \quad (11)$$

The steps of kernel PCA dimensionality reduction can be summarised as:

1. Construct the kernel matrix K from the training data set $\{x_i\}$ using Eq. (3);
2. Compute the Gram matrix $\tilde{K}$ using Eq. (10);
3. Use to solve for the vectors ai (substitute K with $\tilde{K}$);
4. Compute the kernel principal components y_j using Eq. (11).

5. Results and discussion

5.1. Load cycles and strain measurements

The load-midspan displacement curves obtained from interrupted tests were presented in **Error! Reference source not found.** and the maximum displacement points (MDPs) at each consecutive load steps were marked. The intercepts of the tangent lines at the MDPs of each loading cycles were denoted as b_1 to b_6, which was used later for state index identification. Every loading cycle (LC) was composed of two phases: a rising load phase (RL) and a decreasing load phase (DL). The initial load cycle, i.e., LC1, showed a linear trend during the RL phase. An observed non-linearity was found at the RL of LC2 after following replicated linear trend as LC1 and the positional offset from the initial point after the DL of LC2 was evident, which was guessed due to the rate-dependent relaxation phenomenon. From LC3, the RL phase indicated a decrease in the stiffness compared with LC1 and LC2, which could be a sign of microcracks damage initiation. This stiffness degradation was further increased in the load cycles, LC4 and LC5, during when the fictitious cracks might generate. Finally, when the beam resistance was maximum with the force of 471.3 N (LC5), gradual degradation with a rise in deflection continued as the localised fictitious cracks propagated and the fibre was yielding, with a comparatively reduced peak load in LC6. It should be noted that the inherent damage was induced under the upper loading cell due to the high contact stress concentration instead of the bending effect.

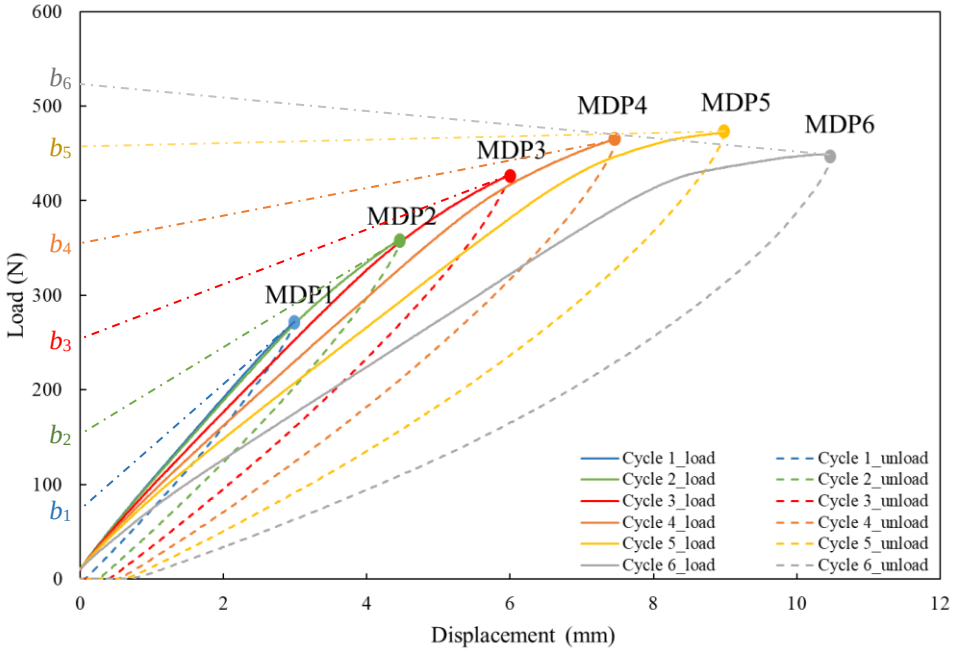

Figure 5: Load-displacement curves of the braided composite beam during interrupted quasi-static test. The Maximum Displacement Point (MDP) at each consecutive load cycles (LC) in interrupted tests are marked. *bi* (*i* =1-6) indicates the intercepts of the tangent lines at the MDPs of loading cycles.

Figure 6(a) and 6(b) showed the strain profiles taken at the MDPs of each load cycle along the embedded DOFS length for LC1 to LC5 and with LC6, respectively. The increase in the strain peak from LC1 to LC3 was constant until a significant strain change occurred at LC4. At LC4, localised peak vibrations around the middle position were visible from DOFS: this abrupt change could be an indication of significant local damage within fibres. At LC5, some dropout points started to appear at around crack locations, which was caused by the spectral shift calculation algorithm due to the low correlation with the reference spectrum [30]. However, during LC1 to LC5, the signal from OF had the capability to go back to the starting point during the unloading, since LC6, the signal was not able to return. The strain configuration measurement indicated the breakage of the optical fibre at LC6. It worth to highlight that although the optical fibre located with a short distance away from the damage location, it still sensitive enough to capture the strain change caused by the damage. Generally, the direct strain outputs revealed qualify distinctions between each step, however, it would be difficult to quantify the damage evolution due to the lack of a proper methodology to deal with all the raw data. Therefore, the proposed smart learning scheme was required to link the raw strain data with the state index determined from the physical performance of the material.

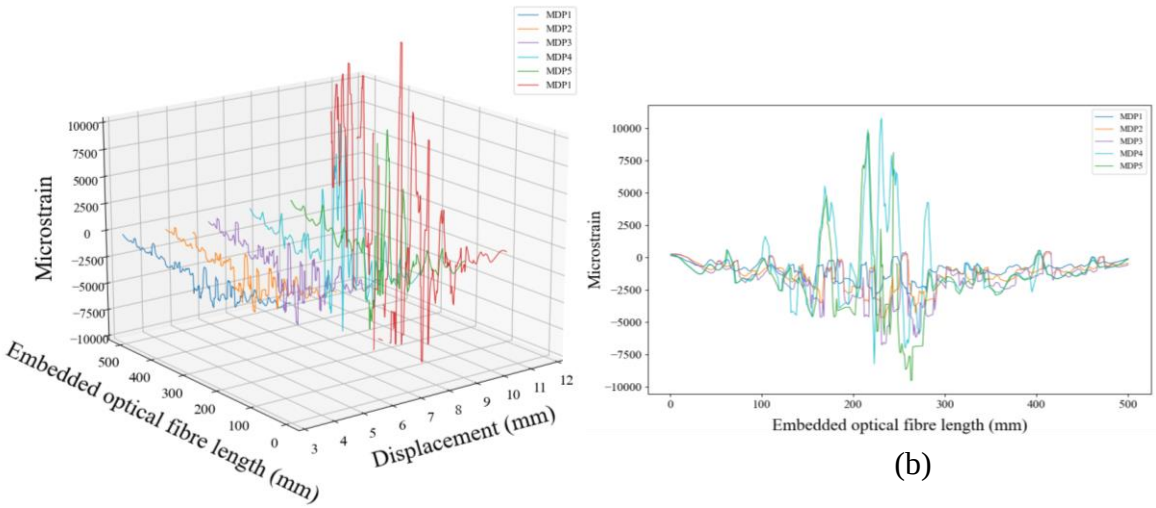

(a) (b)

Figure 6: Strain distributions along the embedded DOFS length at the MDPs of each load cycles: (a) MDP1 to MDP6 and (b) MDP1 to MDP5.

5.2. Damage label projection and propagation

Based on the load-displacement performance of the specimen under different load cycles, the intercept of the tangent line at MDP of the i^{th} cycle was defined at b_i, considering both the physical influences of the failure load and failure displacement. Such as, the intercepts of the tangent line at MDPs decreased from LC1 to LC6, and switched to negative at LC6. Six damage classes (defined as C_i) were described by normalising the intercept of the tangent lines at the MDPs at the i^{th} cycle, as explained in Eq. (12). The values of the six damage classes were shown in Table 2, indicating the damage state at the last loading point in a certain load cycle.

Table 2 Defined damage classes (C_i)

C_1	C_2	C_3	C_4	C_5	C_6
0	0.2043	0.3383	0.497	0.9566	1

$$C_i = \frac{b_i - \min(b)}{\max(b) - \min(b)}, i = 1,2,\cdots,6 \tag{12}$$

where b_i is the intercept of the tangent line at MDP in the i^{th} cycle. According to the DOFS's acquisition rate of 1 Hz, a datapoint was described as the strain distribution along the embedded DOFS length at the i^{th} second, where the upper range of i was 1179 to cover the whole load cycles. The strain nephogram of LC1 to LC6 were illustrated in Figure 8(a), where the starts and ends of each cycle were marked with red dash lines and the MDP locations in the datapoint were noticed with black dash lines. A total of 500 points along the embedded DOFS length direction was mapped in Figure 8(a). The labels of the datapoint (defined as a_i) were defined as the proportion coefficient of the damage classes (C_i). Hence, a state index (defined as S_{index}) can be determined by summing up the class values after multiplying each proportion coefficient, as explained in Eq. (13):

$$S_{index} = \sum_{i=1}^{6} C_i a_i, i = 1, 2, \ldots, 6. \tag{13}$$

The purpose of the label spreading was to propagate the initial few labels that were artificially assigned at the MDPs to the whole load cycles and compare the similarity of all the other datapoints and then assign the labels to them. In this case, the state index could be calculated for all the datapoints based on the raw strain distributions. All the datapoints were labelled by KNN kernel with label spreading algorithm. Subsequently, the label values will be changed in iterations and spreading to all the unlabeled data. The prerequisite of the label spreading algorithm was that the datapoints at the MDPs were given initial labels with a_i equals to 1 where i was the corresponded load cycle and 0 in other labels. For example, at LC3, the labels of the datapoints were $a_3 = 1$ and $a_{1,2,4,5,6} = 0$. The visualisation of the labels predicted by the label spreading algorithm was shown in the Figure 8(b), since the value of C_1 is 0 which did not affect the state index, therefore C_1 was not plotted. It can be seen that the label distributions along the datapoints in damage class 2 (C_2) and damage class 3 (C_3) exhibited some similarity, this was also happened to C_4 and C_5, however, C_6 behaved differently due to the OF breakage. The label performance could be evident by the strain nephogram in Figure 8(a).

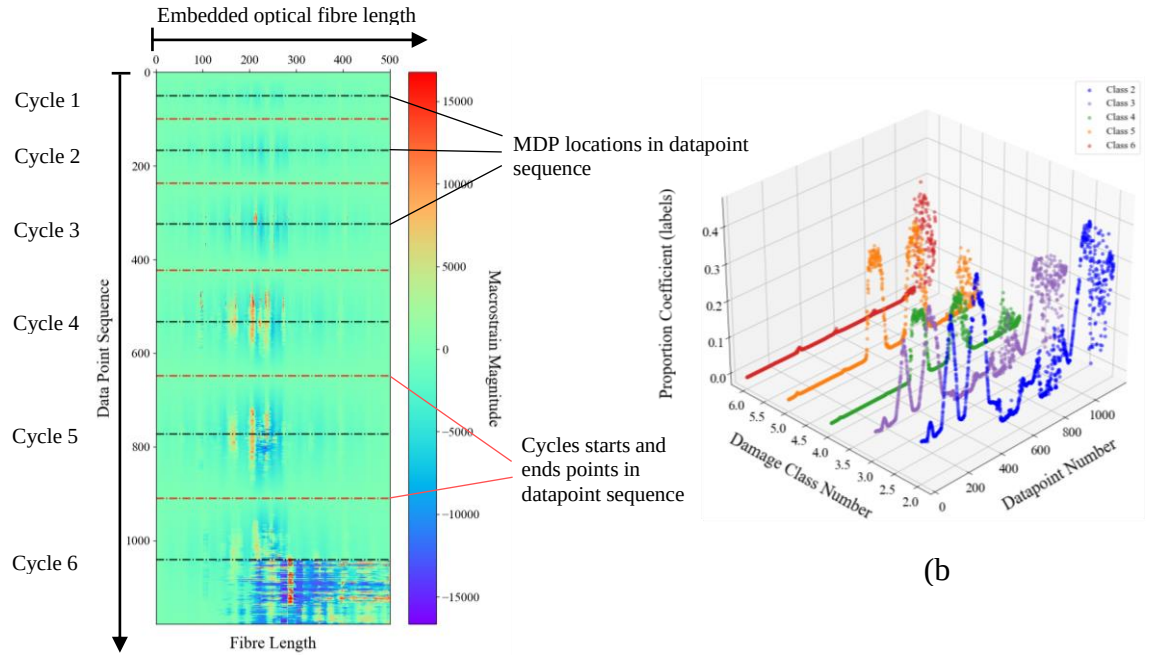

(a) (b

Figure 8: (a) Strain nephogram along the embedded optical fibre length of LC1 to LC6 obtained from DOFS measurement: the starts and ends of each cycle were marked with red dash lines and the MDP locations in the datapoint sequence were marked with black dash lines; (b) visualization of the labels predicted by the label spreading algorithm.

Figure 9 shows the state index projected by the labels given by the label spreading algorithm. The blue points were the state index calculated by the initial labels, and the red points were the predicted values of the state index by KNN kernel. Since the proportion fractions of artificially labelled points can be altered, their label values were changed in each alteration until convergence reached. The other colourful markers shown in Figure 9 were automatically propagated by the algorithm. The fitting results reflected the damage degradation of different load cycles. The state index plots at LC1 and LC2 were symmetric and from LC3, a slight unsymmetric behaviour was found which was guessed due to the inherent microcracks in the matrix which required further detailed studies. The state index scattered around the peak of LC4 and LC5 indicating the potential noise impact due to the crack propagation. In LC6, the state index was collapsed. The predictions of state index were verified by the experimental observations, taken at the end of each load cycle with a travelling microscope, as shown in Figure 3(b). It can be seen that there was no evident crack before LC3, however, from LC4, a dominant crack of approximately 5 mm and a side crack of around 3 mm which was located close to the dominant crack were evident from the sample. In LC5 and LC6, the two cracks continuously grew in dimension and induced obvious vibration in the datapoints, as shown in Figure 8(a). It was guessed that the cracks were propagated to the location of the OF and resulted in the OF damage finally. In general, the state index and labels prediction had a good agreement with the experimental observations, which demonstrated the accuracy and effectivity of the study.

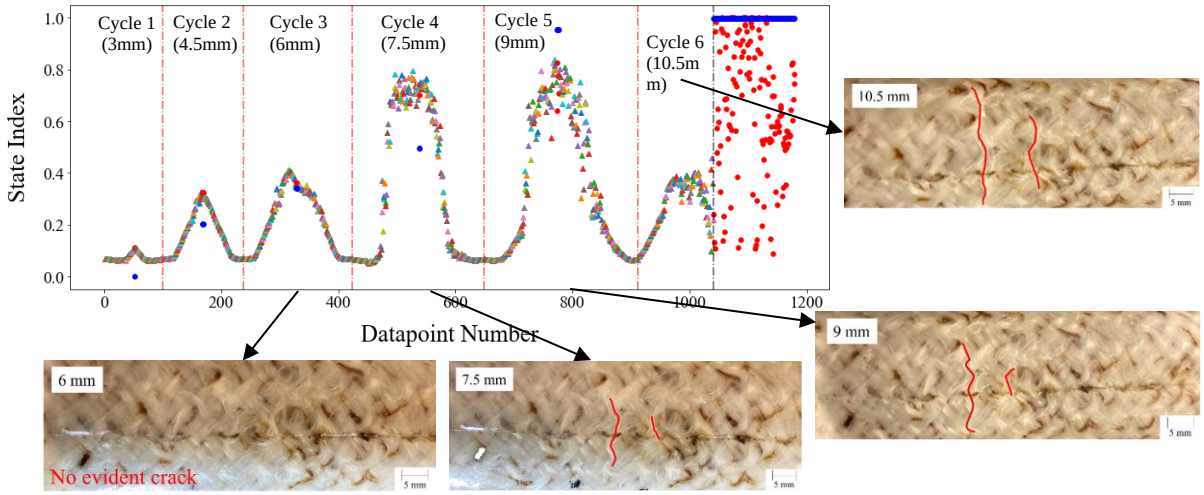

Figure 9: State index projected by label spreading algorithm: blue points were the state index calculated by the initially given labels; red points were the fitted results of datapoints given by the KNN kernel algorithm. The images showed the damage happened at the centre of the beam under the loading cell taken by the travelling microscope, with the red lines indicated the crack length.

5.3. Data regression and validation

In section 5.2, the state index and labels were created for all datapoints and associated with the experimental performance. To achieve the purpose of using a specific datapoint to predict the state index herein, an eight-layer DNN architecture was constructed to fit the labels of all the datapoints. The datapoints from LC1 to LC5 were considered as datasets, it should be noted that the one from LC6 was excluded due to the significant noise from OF breakage. The general schematic of the DNN network used for predicting labels was shown in Figure 10. The input of the neural network was the data contained in a datapoint, and it was then propagated to the three Dense layers (Dense layer 1 to Dense layer 3) which contained 256, 128, and 64 kernels separately. After being propagated, the variables in the Dense layer 3 were transferred to six branches. In each branch, another three Dense layers were used to map the relationship between the variables in Dense layer 3 and the output labels, with the number of kernels listed. Two kinds of activation functions, named “Sigmoid” and “ReLU” were used in the red box below Dense in Figure 10. The biases were used in each layer, initialised as 0. For the weights in the kernels, the initialiser of “glorot uniform” was employed. The superparameters were set as learning

rate of 0.005, rho of 0.95, epsilon of 1e-07 and the optimiser “Adadelta” was used in the model. “Mean squared error” function was chosen to calculate the metrics and the losses of the labels. The data was fitted by the model and updated in a batch size of 32. The outputs of the DNN architecture were the predicted labels, which were then used to predict the state index by utilising Eq. (13).

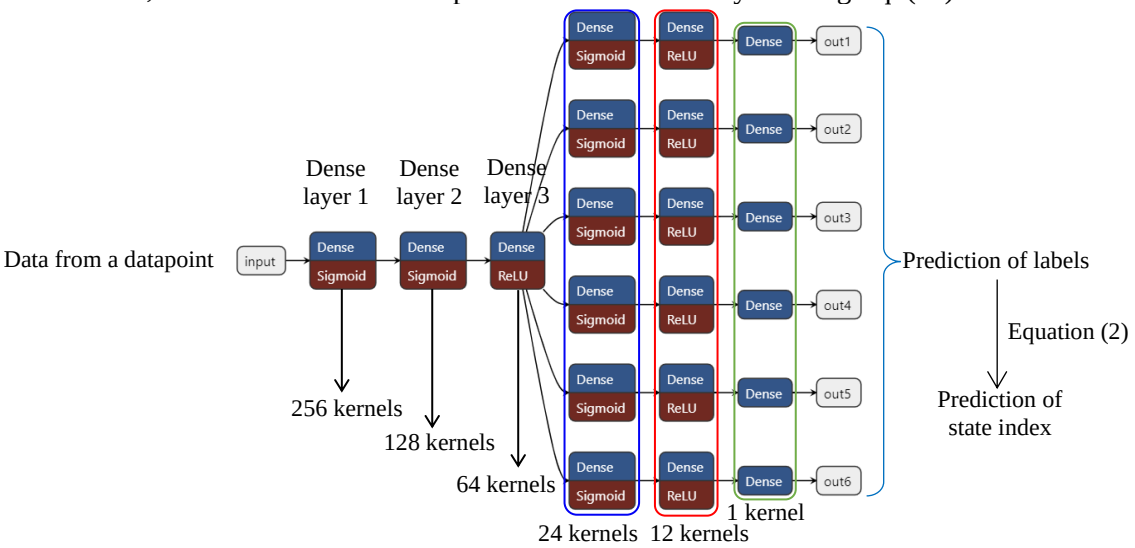

Figure 10: General schematic of a DNN architecture for predicting labels. The number of kernels were listed below each hidden layer and the choice of activation functions was shown in the red box below the Dense.

The dataset of the model was split as 50 datapoints for prediction, 100 datapoints for validation and the remaining datapoints for training. In the learning process, only the training dataset was used to update the variables of the model and the validation dataset was performed after the variable updates of each batch. Once the model was trained, all the datasets will be used to verify the accuracy of the model. The order of the datapoints in the dataset was shuffled to ensure that the model could learn all the process in the load cycles stochastically. To avoid the so-called “overfitting” effects may be caused by the choice of dataset split, six cross validations were performed to verify the adaptivity of the model to all the datapoints. The split of dataset for cross validations was shown in the Figure 11. The fitting performances of the model on all datasets in shuffled order and normal order under six cross validations were plotted in Figure 12. The data between black and blue dotted line was the prediction dataset and the data between blue and red dotted line was the validation dataset. Generally, the model can fit all the training datasets well, although the accuracy was comparably low for the validation and prediction datasets. This was because the validation and prediction datasets were not used to update the variables in the model during the training process resulting in the underfitting of the datapoints. As it can be seen, the state index of the datapoints could be fitted uniformly over all load cycles and exhibited no difference over the cross validations.

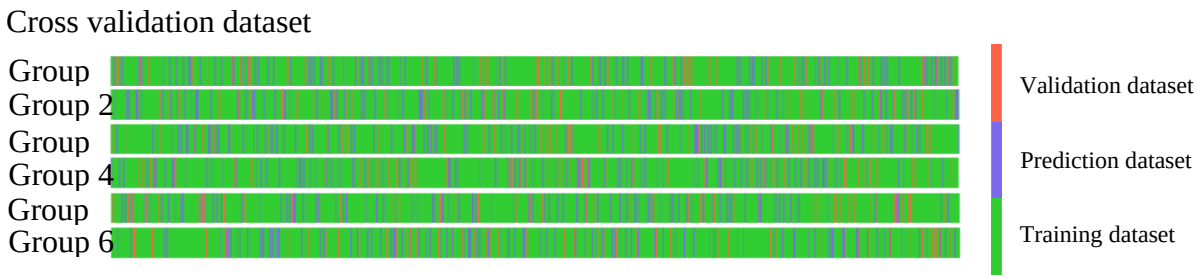

Figure 11: Scheme diagram of the split of dataset for cross validations.

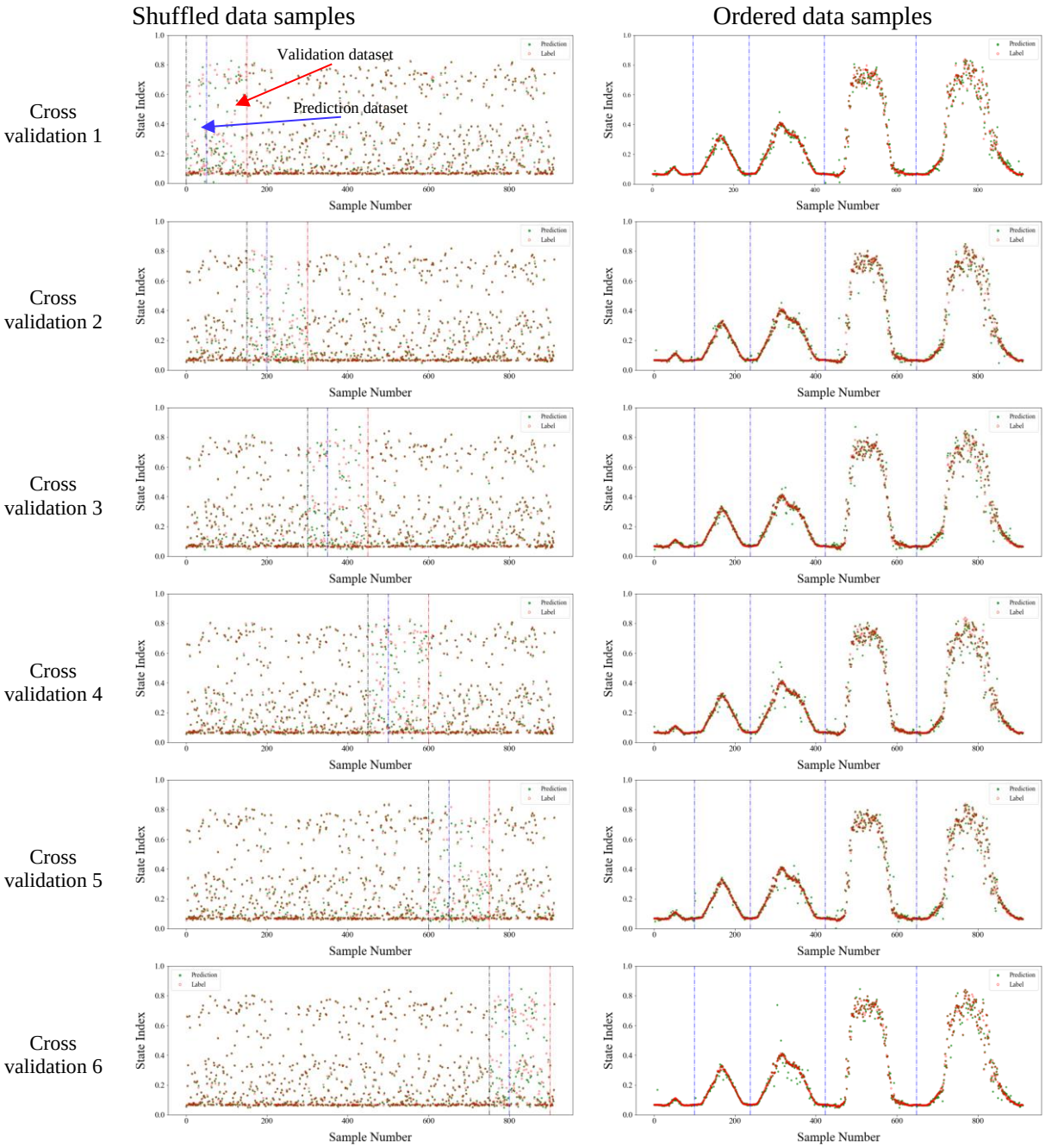

Figure 12: Cross validation of the DNN, the left and right indicate the shuffled and ordered data samples. The data between black and blue dotted line are the prediction dataset and the data between blue and red dotted line are the validation dataset.

5.4. Damage state visualisation and identification in the feature space

By data analysis in Section 5.2 and data regression in Section 5.3, the state index projected by label spreading algorithm on the basis of raw datapoints can be successfully regressed by DNN models. It is also very important to visualise and identify the loading situations and damage state to assist the intermittent inspection and maintenance activities in the practical engineering work.
Consequently, the labels projected by the label spreading algorithm were decomposed to a three-dimensional feature space by kernel principal component analysis. The decomposed dimensions were referred as components which retained the maximal integrity of the intact data information while reduce the redundancy. Three components were extracted from the six labels of datapoints of six load

cycles. All the datapoints were used to form the transformation matrix and the visualisation of the datapoints in the transformed space, as shown in Figure 13(a). In this way, the loading and unloading processes and data pattern changes of the specimen could be easily identified. In Figure 13(a), the data components changed continuously from LC1 to LC3 with the data of the loading and unloading cycles along the same path in the component space. After LC3, the data showed a pattern change in the load cycles, and they were no longer in the same path as LC1 to LC3 which indicated an irreversible damage occurred in the structure. In the unloading process of LC4 and LC5, the data cannot recover to the original position of that cycle even at the ends of unloading. In LC6, the data showed random and irregular patterns which was caused by the DOFS breakage failure, the data scattered in the space which was out of the previously presented path.

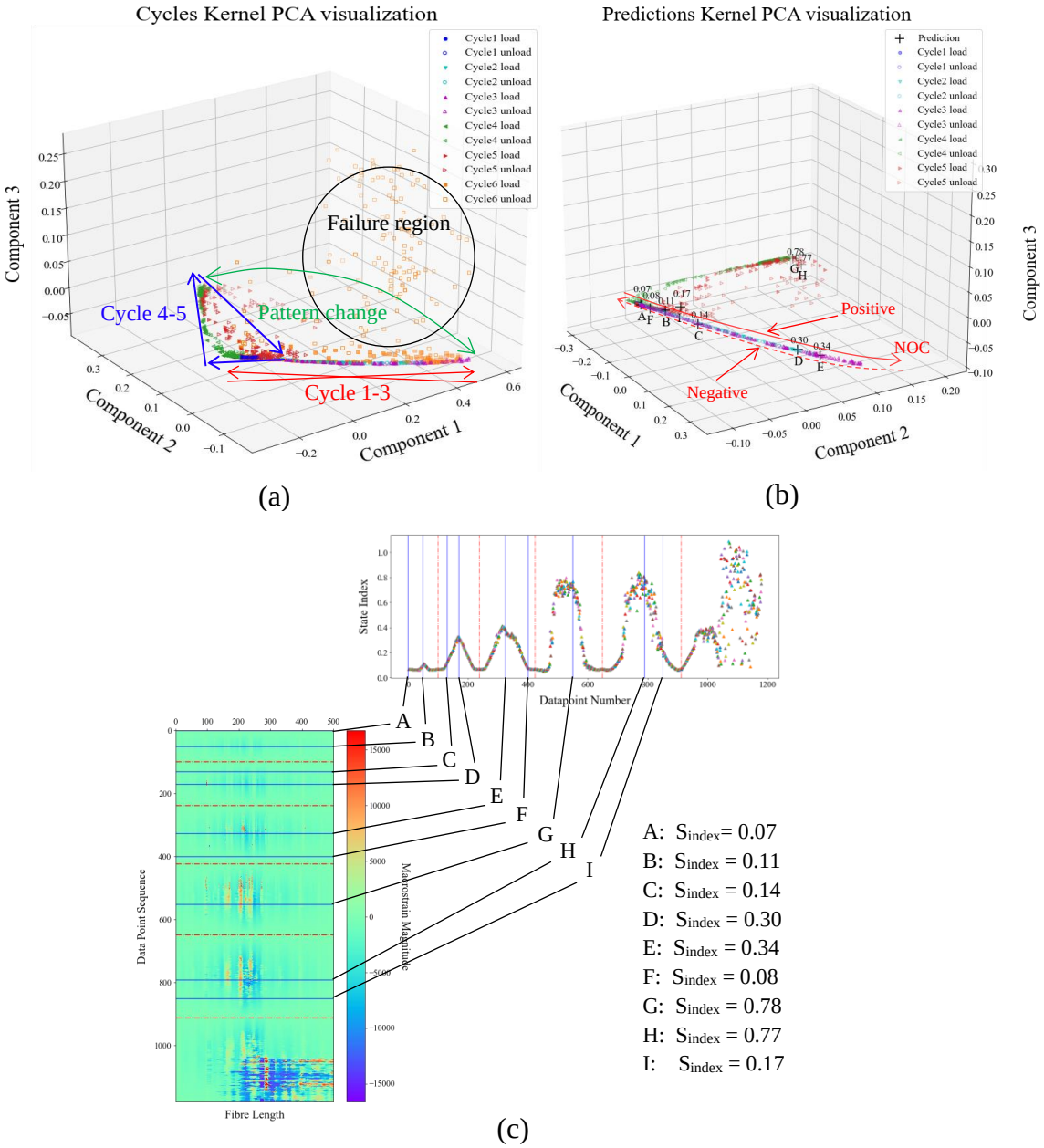

Figure 13: (a, b) Kernel PCA analysis of propagated labels; (c) state index and position of A~I in load cycles.

To better interpret and implement this methodology for SHM application, a group of data was selected randomly from different load cycles to examine the damage states. The selected data was shown in Figure 13(c), which was spread to the strain nephogram to exhibit its position e.g., point A was the

start of LC1; point C was picked in the loading of LC2; point G was picked in the unloading of LC4. The state index values predicted by DNN were also listed in Figure 13(c). These points were visualised in the feature space for damage identification and verification in Figure 13 (b). A normal operating curve (NOC) was defined to be the path of LC1 to LC3 where no damage was considered. The direction of solid line plotted in the Figure 13(b) was defined as the positive direction of NOC and vice versa for the dotted line. If the presence of data followed the positive direction of NOC, the state index would also increase, which indicated that the sample was under loading stage, such as, point A to point B in LC1 and point C to point D in LC2, and vice versa. The position of the data in NOC was also associated with the magnitude of loading, i.e., the positions of data in MDPs were at the furthest position from the initiation, for example, point B was at the furthest position in data of LC1.

It could also be found that the presenting order of damaged data would be different or along different path in the feature space, such as, point G, H, and I, which could be regarded as a pattern change of strain measurement. It should be pay attention that point I was not on the NOC and the data at the end of LC5 could not return to original position (point A). Thus, the damage state of the specimen could be identified by observing the position and sequence of datapoints in the feature space.

6. Conclusions

This paper presented a general data driven based prediction methodology to auto-detect state index in a Structural Health Monitoring (SHM) system by utilising Distributed Optical Fibre Sensing (DOFS) for strain measurement within a composite braided beam structure under six three-point bending loading-unloading cycles. Instead of designing a large set of experiments in various scenarios and numerical simulations to compensate for the data driven models, this study employed semi-supervised learning from a realistic test setup with merely six load cycles. The diagram of this methodology included a combination of preliminary defined state index based on experimental behaviours, and label projection given by the label spreading algorithm and KNN kernel algorithm, as well as state index prediction and validation with a DNN architecture. The damage state of the sample within different load situations was able to be visualised and identified in the feature space. Based on the above studies, the following conclusions can be drawn:

1. The DOFS located with a vertical distance of approximately 5.3 mm has demonstrated the sensitivity of detecting the strain changes within the different loading cycles. When the crack propagated to the position of DOFS, the breakage of the DOFS has resulted in a significant amount of noise.
2. The state index and labels projected by label spreading algorithm can well fit and corelate with the experimental observations with only a few artificially labelled datapoints, which demonstrated the feasibility of the proposed methodology. These labels can then be successfully fitted by the proposed DNN architecture, and the subsequent state index of the sample can be accurately predicted by merely raw strain datapoints.
3. By decomposing the labels of datapoints with the Kernel Principal Component Analysis, the positions of datapoints in the feature space combined with state index can be used to verify the presented damages and loading conditions of the sample, which can help to implement structural health monitoring of structures.
4. In SHM of the composite braided beam with DOFS, this technology can examine the presented damage and load state by learning six progressive cycles. Upon this study, this technology can be exploited to other engineering cases that satisfy the following two requirements: a) damage only occurred and propagated in the specific area of the sample, b) the loads are repeatedly and gradually increasing. In this case, the measured raw data (e.g., strain) would alter continuously in patterns, making it possible to be decomposed to feature space and the pattern change would follow an explicit routine associated with the load magnitude. Meanwhile, any data presence deviated from this routine indicated potential damage in the sample.

Overall, the proposed methodology offers a novel perspective on SHM data processing, which is crucial for automatic real-time monitoring and alarming of SHM systems as well as long-term analysis of structures based on its long-term performance data. This methodology also serves for other types of

SHM techniques, i.e., sensors. In the future work, it may be worth to examine the feasibility of this methodology with combined load cases.

Acknowledgements

The authors would like to acknowledge the support of the Catapult funding's financial support (Grant reference: 160080 CORE HVMC(WMG)), which made the completion of this project possible. The authors are grateful to Dr Yifei Yu for providing ODiSI-B system, Dr Remy Guillaume for micro-CT X-ray scanning and also appreciate the technical support from Mr Ian Shannan from LUNA Ltd.

References

[1] Yuan F-G, Zargar SA, Chen Q, Wang S. Machine learning for structural health monitoring: challenges and opportunities. Proc SPIE 2020;1137903:2.

[2] Farrar CR, Worden K. Structural Health Monitoring: A Machine Learning Perspective. Wiley; 2013.

[3] Perera R, Torres L, Ruiz A, Barris C, Baena M. An emi-based clustering for structural health monitoring of NSM FRP strengthening systems. Sensors 2019;19.

[4] Sierra-Pérez J, Torres-Arredondo MA, Cabanes G, Güeme A, Mujica LE. Structural Health Monitoring by Means of Strain Field Pattern Recognition on the basis of PCA and Automatic Clustering Techniques Based on SOM. IFAC-PapersOnLine 2015;48:987–92.

[5] Bao Y, Tang Z, Li H, Zhang Y. Computer vision and deep learning–based data anomaly detection method for structural health monitoring. Struct Heal Monit 2019;18:401–21.

[6] Bernal D. Load Vectors for Damage Localization. J Eng Mech 2002;128:7–14.

[7] Gu Z, Liu Y, Hughes D, Ye J, Hou X. A parametric study of adhesive bonded joints with composite material using black-box and grey-box machine learning methods: Deep neuron networks and genetic programming. Compos Part B Engineering 2021;108894.

[8] Hay TR, Royer RL, Gao H, Zhao X, Rose JL. A comparison of embedded sensor Lamb wave ultrasonic tomography approaches formaterial loss detection. Smart Mater Struct 2006;15:946.

[9] Min J, Park S, Yun CB, Lee CG, Lee C. Impedance-based structural health monitoring incorporating neural network technique for identification of damage type and severity. Eng Struct 2012;39:210–20.

[10] Selva P, Cherrier O, Budinger V, Lachaud F, Morlier J. Smart monitoring of aeronautical composites plates based on electromechanical impedance measurements and artificial neural networks. Eng Struct 2013;56:794–804.

[11] Moharrami H, Khaji N, Abourayan A, Sami M, Avci O, Mehrjoo M, et al. Damage detection of truss bridge joints using artificial neural networks. Expert Syst Appl 2008;35:1122–31.

[12] Liu YY, Ju YF, Duan CD, Zhao XF. Structure damage diagnosis using neural network and feature fusion. Eng Appl Artif Intell 2011;24:87–92.

[13] Park S, Lee J-J, Yun C-B, Inman DJ. Electro-Mechanical Impedance-Based Wireless Structural Health Monitoring Using PCA-Data Compression and k-means Clustering Algorithms: J Intell Mater Syst Struct 2007;19:509–20.

[14] Jiang X, Zhang X, Zhang Y. Piezoelectric Active Sensor Self-Diagnosis for Electromechanical Impedance Monitoring Using K -Means Clustering Analysis and Artificial Neural Network. Shock Vib 2021;2021.

[15] Rufai O, Gautam M, Potluri P, Gresil M. Optimisation of optical fibre using micro-braiding for structural health monitoring. J Intell Mater Syst Struct 2019;30:171–85.

[16] Sánchez DM, Gresil M, Soutis C. Distributed internal strain measurement during composite manufacturing using optical fibre sensors. Compos Sci Technol 2015;120:49–57.

[17] Huang C, Bao X, Zeng X, Arcand A, Lee-Sullivan P. Simultaneous temperature and strain monitoring of composite cure using a Brillouin-scattering-based distributed fiber optic sensor. Smart Struct. Mater. 2001 Sens. Phenom. Meas. Instrum. Smart Struct. Mater., vol. 4328, SPIE; 2001, p. 70.

[18] Kang HK, Kang DH, Bang HJ, Hong CS, Kim CG. Cure monitoring of composite laminates using fiber optic sensors. Smart Mater Struct 2002;11:279–87.

[19] Takeda N, Okabe Y, Mizutani T. Damage detection in composites using optical fibre sensors. Proc Inst Mech Eng Part G J Aerosp Eng 2007;221:497–508.
[20] Sen D, Aghazadeh A, Mousavi A, Nagarajaiah S, Baraniuk R, Dabak A. Data-driven semi-supervised and supervised learning algorithms for health monitoring of pipes. Mech Syst Signal Process 2019;131:524–37.
[21] Kreger ST, Soller BJ, Gifford DK, Froggatt ME, Wolfe MS. High Resolution Distributed Strain or Temperature Measurements in Single-and Multi-Mode Fiber Using Swept-Wavelength Interferometry. Optics InfoBase Confer 2006.
[22] Arhant M, Meek N, Penumadu & D, Davies P, Garg & N. Residual Strains using Integrated Continuous Fiber Optic Sensing in Thermoplastic Composites and Structural Health Monitoring. Exp Mech 2018;58:167–76.
[23] Lu X, Thomas PJ, Hellevang JO. A review of methods for fibre-optic distributed chemical sensing. Sensors 2007;27:223–5.
[24] Bao X, Chen L. Recent progress in distributed fiber optic sensors. Sensor 2012;12:8601–39.
[25] Singh A, Reynolds N, Keating EM, Barnett AE, Barbour SK, Hughes DJ. Three-point flexural performance of tailor-braided thermoplastic composite beam structures. Compos Struct 2021;260.
[26] Sutherland FR. Learning with local and global consistency. Ann R Coll Physicians Surg Can 1997;30:33–4.
[27] Tran-Ngoc H, Khatir S, Ho-Khac H, De Roeck G, Bui-Tien T, Abdel Wahab M. Efficient Artificial neural networks based on a hybrid metaheuristic optimization algorithm for damage detection in laminated composite structures. Compos Struct 2021;262:113339.
[28] Sharma P, Singh A. Era of deep neural networks: A review. 8th Int Conf Comput Commun Netw Technol ICCCNT 2017 2017;40222.
[29] Wang Q. Kernel Principal Component Analysis and its Applications in Face Recognition and Active Shape Models. ArXiv 2012;1207.
[30] Rufai O, Chandarana N, Gautam M, Potluri P, Gresil M. Cure monitoring and structural health monitoring of composites using micro-braided distributed optical fibre. Compos Struct 2020;254.